Materials Science & Engineering A 916 (2024) 147395

Contents lists available at ScienceDirect

Materials Science & Engineering A

journal homepage: www.elsevier.com/locate/msea

Effect of thermomechanical processing on mechanical properties and the microstructure of binary Al-Ce alloy

Gaurav Singh [a], Humphrey Wara Odhiambo [b], Mohamad Hasan Bin Tasneem [a], Gaoyuan Ouyang [b,c,**], Monica A. Soare [d], Jun Cui [b,c], Ralph E. Napolitano [b], Catalin R. Picu [a,*]

[a] Department of Mechanical, Aerospace and Nuclear Engineering, Rensselaer Polytechnic Institute, Troy, NY, 12180, USA
[b] Department of Materials Science & Engineering, Iowa State University, Ames, IA, 50011, USA
[c] Division of Materials Sciences and Engineering, Ames National Laboratory, Ames, IA, 50011, USA
[d] General Electric Global Research, Niskayuna, NY, 12309, USA

ARTICLE INFO

Keywords:
Al-Ce alloy
Mechanical properties
Microstructure
Fracture toughness
Extrusion

ABSTRACT

A new generation of Al alloys based on the Al-Ce system, with microstructure and properties weakly sensitive to elevated temperatures, is being developed for applications such as thermal engine blocks and supersonic aircraft fuselage components. Cast Al-Ce binary alloys with 4, 10 and 16 wt% Ce were produced by slab casting and further processed by extrusion. Extrusion produces a highly refined microstructure resulting in a twofold increase in strength (tensile strength of 228 MPa at room temperature). We show that the Al-10Ce is highly stable (more than 99 % strength retention after 300 °C 100 h exposure), far superior to high temperature grade Al alloy AA2618. The extruded Al-10Ce also shows a room temperature ductility of more than 20 %, with a fracture toughness of 55.42 kJ/m^2 that does not degrade after high temperature exposure (97.6 % toughness retention after 300 °C 100h exposure). Results from testing at different temperatures are also reported.

1. Introduction

Al alloys are broadly used in subsonic aircraft design due to their high specific strength and corrosion resistance. Supersonic aircrafts are subjected to elevated temperatures due to aerodynamic friction. The temperature of critical components of the skin and fuselage increases linearly with the Mach number and reaches values of 300 °*C* at Mach 3 and is larger than 450 °*C* at Mach 4. This precludes the use of current Al alloys, such as the precipitate hardened AA2XXX and AA7XXX series, as their properties degrade rapidly above ~220 °*C* [1]. The main strengthening mechanism of precipitate hardening is disabled at higher temperatures due to precipitate coarsening and dissolution [2]. A current solution is to use more thermally stable but heavier alloys, e.g. Ti-based, for such applications [3].

A new generation of temperature-resistant Al alloys based on the Al-Ce system is considered as a potential solution for high temperature airframe applications [4–6], enabling replacement of selected Ti alloy components and realization of significant weight reduction that reflect in reduced energy consumption and reduced emissions. The goal of this material development effort is to obtain microstructures stable enough to retain the room temperature yield strength, tensile strength and fracture toughness [7–9] upon exposure to elevated temperatures (300 °*C*).

Ce is the most abundant rare earth metal, currently lacking high-volume applications [10,11]. In the literature, it is described as one of the potential candidates for acting as a primary alloying element in Al alloys [12]. Within the composition range considered here (≤ 16 wt% Ce), microstructures generally involve the $Al_{11}Ce_3$ intermetallic phase within the Al (fcc) majority phase. For the purposes of achieving high strength, a uniform dispersion of fine intermetallics is desirable [17]. With Ce exhibiting vanishing solubility and very low diffusivity in the Al (fcc) phase, precipitation strengthening through conventional diffusional aging processes is precluded. However, if fine Ce-bearing intermetallic dispersions can created through other means, these are likely to be highly stable at elevated temperatures since coarsening processes would also be very sluggish [13–16]. In this work we examine the potential for using casting and thermomechanical processing to achieve the desired microstructures and corresponding high temperature

* Corresponding author.
** Corresponding author. Department of Materials Science & Engineering, Iowa State University, Ames, IA, 50011, USA.
E-mail addresses: gaoyuan@iastate.edu (G. Ouyang), picuc@rpi.edu (C.R. Picu).

https://doi.org/10.1016/j.msea.2024.147395
Received 28 July 2024; Received in revised form 13 October 2024; Accepted 14 October 2024
Available online 16 October 2024

properties.

Al-Ce alloys in the near-eutectic range (5–20 wt% Ce) exhibit excellent castability and resistance to hot tearing and cracking [21–24] with off-eutectic microstructures containing the expected primary phases, typically dendritic Al (fcc) for hypoeutectic or faceted script-like or plate-shaped $Al_{11}Ce_3$ particles for hypereutectic alloys. In either case, the nonuniform spatial distribution of intermetallic does not lead to the most efficient strengthening [13–15]. Given the potential utility of Al-Ce alloys in high temperature applications, conventionally cast alloys require further processing for microstructural refinement to enable suitable performance in applications requiring high strength under prolonged exposure to elevated temperatures.

Forging, rolling and extrusion, as well as severe plastic deformation (SPD) processes, such as high-pressure torsion and equi-channel angular pressing, have been used extensively to produce microstructural refinement in metallic materials [16], however, processing of Al-Ce alloys by these methods has received limited attention.

Zhang et al. [26] studied the effect of heat treatment on the mechanical properties of an Al-9Ce alloy produced by casting in a heated (300 °C) graphite mold followed by 85 % reduction in thickness by cold rolling. Two important effects of cold rolling were identified. First, rolling of the hypoeutectoid structure resulted in flattening of the primary dendritic Al (fcc) phase, producing a laminar composite overall structure consisting of alternating layers of primary Al (fcc) and a fine two-phase eutectic constituent (Al (fcc) + $Al_{11}Ce_3$) which itself consists of fine lamella or rods of $Al_{11}Ce_3$. Enhanced ductility and toughness were attributed in part to this composite structure, where the large Al (fcc) grains provide high capacity for plastic deformation and the fine composite structure in the eutectic provides a mechanism for ductile blunting of microcracks potentially emanating from the brittle $Al_{11}Ce_3$ phase. Second, the cold rolling process resulted in the refinement of the eutectic $Al_{11}Ce_3$ particles through mechanical fracture along with preferential alignment of the resulting particles along the rolling direction. It was asserted that this particle alignment contributes to the observed increase in strength, presumably through more efficient load transfer of the aligned composite structure. Post-deformation heating further showed significant Al recrystallization at 300 °C and substantial grain growth at 400 °C, but these changes had little effect on mechanical properties, which are largely dictated by the morphology and distribution of the hard/brittle phase. Stanislav et al. showed the effect of high-pressure torsion on the microstructure and tensile properties of Al-9Ce. The process leads to the formation of nanograins and a large increase of the yield stress and tensile strength [4,17].

While reports of investigations into the influence of extrusion processing on mechanical properties of Al-Ce alloys are limited, significant promise has been shown. Indeed, extrusion of binary Al-Ce alloys has been reported to produce ultimate/yield strengths of 400/340 MPa, competitive with high strength wrought aluminum alloys (e.g. AA2618) and with far lower extrusion ratios (i.e. 3:1 as compared with 10:1) [18]. Other reports of extrusion in Al-Ce (based) alloys are seemingly confined to processing of dilute alloys (≥99 % Al) for applications such as electrical conductors [19,20].

With clear evidence that the mechanical properties of Al-Ce alloys are largely attributable to the fraction, morphology, and spatial distribution of the intermetallic $Al_{11}Ce_3$ particles and that these can be substantially controlled through Ce content and processing (solidification, deformation, and heat treatment), the present work focuses on the thermal stability of cast Al-4Ce, Al-10Ce and Al-16Ce and extruded Al-10Ce alloy (all percentages in wt%). Microstructures are characterized using SEM, XRD, and EBSD and mechanical properties are measured at ambient and elevated temperatures by uniaxial tensile testing and fracture toughness testing. We examine microstructural refinement, thermal stability, strengthening mechanisms, and the fracture toughness of cast and extruded Al-10Ce alloys before and after heat treatment. We conclude that extrusion produces significant precipitate and grain refinement, and the microstructure is stable upon exposure to 300 °C for durations up to 100 h, with minimal reduction of mechanical properties associated with heat treatment.

2. Experimental

2.1. Materials and processing

Al-Ce ingots with 4, 10 and 16 % Ce were produced by slab casting (graphite open slab mold) at casting temperature of 850 °C and a mold temperature of 400 °C. The eutectic composition Al-10Ce was selected for extrusion. 25.4 mm diameter as-cast rods were reduced to 9.5 mm diameter by extrusion at 300 °C. At the onset of the experiment, the heating rate of the extrusion furnace chamber is 10 °C/min using Innovare LMS extrusion press. An equilibration at the target temperature for 30 min is applied before extrusion; extrusion is performed by adjusting the pressure from 11.6 ksi (80 MPa) to 81.4 ksi (561 MPa) within 5 min. At the end of extrusion, a fan is used to cool the extruded rod to room temperature, after which the rod is ejected.

The mechanical properties were measured in the as-cast (AC) and cast/extruded (CE) conditions and also in the corresponding heat treated conditions (AC-10, AC-100, CE-10, CE-100), where the number indicates hours at 300 °C. Table 1 summarizes the tested alloys and conditions used in the present study along with the naming convention established for the remainder of this communication.

2.2. Tensile and fracture experiments

Tensile specimens were machined using CNC per the ASTM E8 standard [21] for all cast, extruded, and heat-treated conditions. The tensile direction is parallel to the extrusion direction. The gauge has rectangular cross-section of dimensions 5 × 6 mm^2 and the gauge length is 52 mm. Tensile tests were performed using an Instron machine (Instron 5969, 50 kN load cell) under quasi-static conditions ($\dot{\varepsilon} = 3 \times 10^{-3}\ s^{-1}$) at room temperature (25 °C). We have used a mechanical extensometer to measure the strain. Three repetitions are performed for each material condition.

Tests at elevated temperatures of 150 °C, 200 °C, 250 °C, 300 °C and 350 °C were performed with the same system, the sample being heated at a rate of 5 °C/s to reach the test temperature, followed by a 300 s hold before the beginning of the test. The deformation of samples tested at elevated temperatures was provided by the machine.

Hardness was measured with a microhardness tester (Qness 60M QATM) with a load of 500 g, with 15 s dwell time [22], in accordance with ASTM E92. At least three samples were tested in each condition, and 10 measurements were made of each sample. The average values are reported here.

Elastic-plastic fracture toughness (J_{Ic}) was measured using an Instron (Instron 5969, 50 kN load cell) uniaxial load frame by single-edge bend testing according to the ASTM E1820 standard [23]. Specimens had dimensions 12 X 6 × 60 mm and the loading span was 50 mm. Prior to testing, fatigue loading with amplitudes of 0.10–0.20 kN, was used to generate a pre-crack extending a length of 1.2 mm from a machined notch, normal to the axial direction of the extruded rods to achieve a standard crack length to width ratio of 0.5.

Table 1
Summary of the alloys and conditions utilized in the present study.

Naming Convention	Description
AC	As - Cast
CE	Cast and extruded
AC-10	As – Cast +300C for 10 h
AC-100	As – Cast +300C for 100 h
CE-10	Cast and extruded +300C for 10 h
CE-100	Cast and extruded +300C for 100 h

2.3. Microstructure characterization

Test specimens for both XRD and metallographic (SEM/EBSD) analysis were prepared by sectioning and grinding with fixed abrasive papers (320, 800, and 1200 grit) followed by polishing with loose abrasive suspension-embedded cloths (alumina and colloidal silica, 5 μm–0.05 μm). XRD patterns were collected using a Panalytical XRD instrument with Cu-K_α radiation between 20^0 to 90^0, with a scan rate of 1^0 per minute. FEI SEM was used for the metallography and fractography studies. Polished planar surfaces were prepared for examination by etching with Kellar's reagent for 10 s whilst fracture surfaces were examined directly, with no further preparation.

EBSD was performed using an Oxford SEM microscope. The respective specimens were polished using diamond and colloidal silica to minimize the surface roughness. The EBSD step size is 0.05 μm for CE, CE-10, and CE-100, and it is 1 μm for as-cast Al-10%Ce. The analysis of EBSD images was performed using MTEX software. The mapping is based on the FCC Al and orthorhombic $Al_{11}Ce_3$.

3. Results

3.1. Phase analysis

The normalized XRD spectra of hypoeutectic (Al-4Ce), eutectic (Al-10Ce), and hypereutectic (Al-16Ce) cast alloys are shown in Fig. 1a. The α-Al phase and $Al_{11}Ce_3$ intermetallic particles are identified in all three alloys. Normalized XRD spectra of as-cast, as-extruded, and extruded and heat treated Al-10Ce eutectic alloy are shown in Fig. 1b. These samples also indicate the presence of α-Al and $Al_{11}Ce_3$ precipitates. In Fig. 1a, the relative intensities of $Al_{11}Ce_3$ peaks in the as-cast samples increase as the Ce concentration increases, as expected. The height of these peaks is essentially invariant upon annealing at 300 °C for 100 h. The highest intensity peaks for α-Al are (111) or (200) in all compositions and material states considered. The intensity of the Al (200) peak decreases after extrusion and heat treatment as compared to as cast Al-10Ce, which indicates the development of (111) texture during extrusion, as discussed further in section 3.2. No evidence of phase transformations is observed during extrusion and heat treatment, illustrating the thermal stability of this alloy, at least with regard to phase composition.

3.2. Microstructural evolution during extrusion and subsequent annealing

3.2.1. Scanning electron microscopy

The microstructure of AC Al-4Ce, Al-10Ce and Al-16Ce is observed by scanning electron microscopy (SEM) and representative micrographs are shown in Fig. 2a-c. The microstructure for Al-4Ce shown in Fig. 2a includes primary Al (fcc) phase, appearing as large dendritic features separated by a two-phase interdendritic eutectic constituent, comprised of Al (fcc) (dark) and $Al_{11}Ce_3$ (light) phases with a fine irregular lamellar structure. The Al-10Ce microstructure presents exclusively the eutectic constituent (Fig. 2b), while the Al-16Ce microstructure includes primary $Al_{11}Ce_3$ phase (light) exhibiting a blocky script-like morphology within the irregular eutectic constituent of Al (fcc) plus $Al_{11}Ce_3$, as shown in Fig. 3c. These observations are consistent with expectations and with the previously published literature on Al-Ce binary alloys [15,24–26]. More uniform and finer microstructures were formed in the Al-10Ce alloy compared to the other two compositions considered. Due to this, we focus the subsequent microstructure characterization on the eutectic Al-10Ce alloy. The intermetallic mean size (lamellar thickness) of Al-4% Ce, Al-10%Ce, and Al-16%Ce is 0.28 μm, 0.24 μm, and 0.60 μm, respectively. The inter-lamellar spacing of Al-4%Ce, Al-10%Ce, and Al-16%Ce is 0.39 μm, 0.65 μm, and 1.98 μm, respectively.

The microstructure of CE, CE-10, CE-100 (Al-10Ce) is shown in Fig. 3. A homogenous and highly refined microstructure was observed after extrusion. Two phases are present: the α-Al (fcc) matrix and the eutectic structure, with the eutectic structure including Al and $Al_{11}Ce_3$ intermetallic. Comparison between Fig.s. 3a and 2b reveals the changes in $Al_{11}Ce_3$ morphology within the eutectic structure associated with the extrusion process. Particles are refined in size and undergo a change of shape from longer plate-like lamellae to shorter lamellae in the extruded condition. In addition, the particles become preferentially aligned with the extrusion direction. These observations are consistent with prior reports of lamellar fragmentation and alignment during cold rolling [27], as previously discussed. This morphology change is expected to influence ductility, a consideration discussed further in section 3.3. The post-extrusion $Al_{11}Ce_3$ particle size within the eutectic constituent appears to be somewhat bimodal, with a small fraction of coarse particles, suggesting that some particles remain unbroken. Fig. 3 further shows that the particle distribution remains unchanged after exposure to 300 °C for 10 h and 100 h since, again consistent with expectations given the low diffusivity of Ce in Al and the correspondingly sluggish particle coarsening. The intermetallic particle mean size (lamellar thickness) of CE, CE-10, and CE-100 is 0.24 μm, 0.19 μm, and 0.21 μm, respectively. The interlamellar distance of CE, CE-10, and CE-100 is 0.36 μm, 0.29 μm, and 0.30 μm, respectively.

3.2.2. Electron backscattered diffraction

Electron backscattered diffraction technique is used to characterize the grain size, grain misorientation, phase fraction, micro strain, and texture in the as cast, extruded and heat-treated Al-10Ce alloy. Fig. 4a–c shows the electron backscattered diffraction (EBSD) maps of Al-10Ce in the CE, CE-10, and CE-100 conditions. The map of the CE sample shows a heterogenous microstructure with different grain sizes in different regions. For example, the grain size of (101) oriented grains is 3.27 ± 2.67 μm, 2.66 ± 0.78 μm, and 3.67 ± 0.76 μm for CE, CE-10, and CE-100

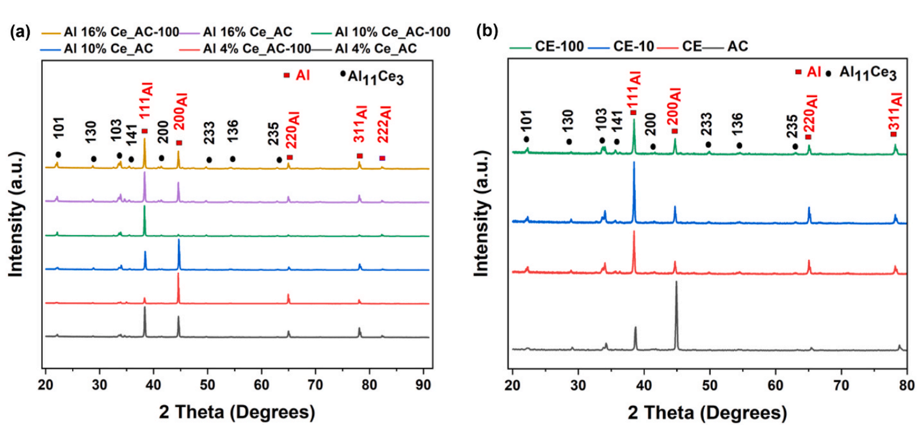

Fig. 1. (a) XRD of Al-4Ce, Al-10Ce, and Al-16Ce for samples AC and AC-100 (b) XRD of AC, CE, CE-10, and CE-100 for Al-10Ce.

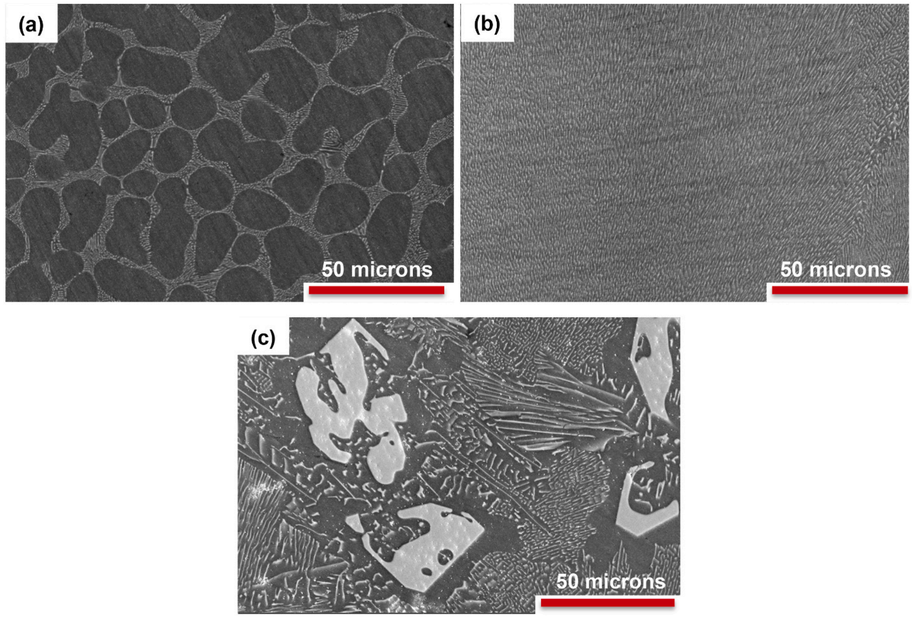

Fig. 2. The microstructure of as-cast: (a) Al-4Ce alloy (black = Al, white = $Al_{11}Ce_3$, lighter shade = eutectic), (b) Al-10Ce eutectic alloy, (black = Al, white = $Al_{11}Ce_3$) and (c) Al-16Ce alloy (black = Al, white = $Al_{11}Ce_3$). (For interpretation of the references to colour in this figure legend, the reader is referred to the Web version of this article.)

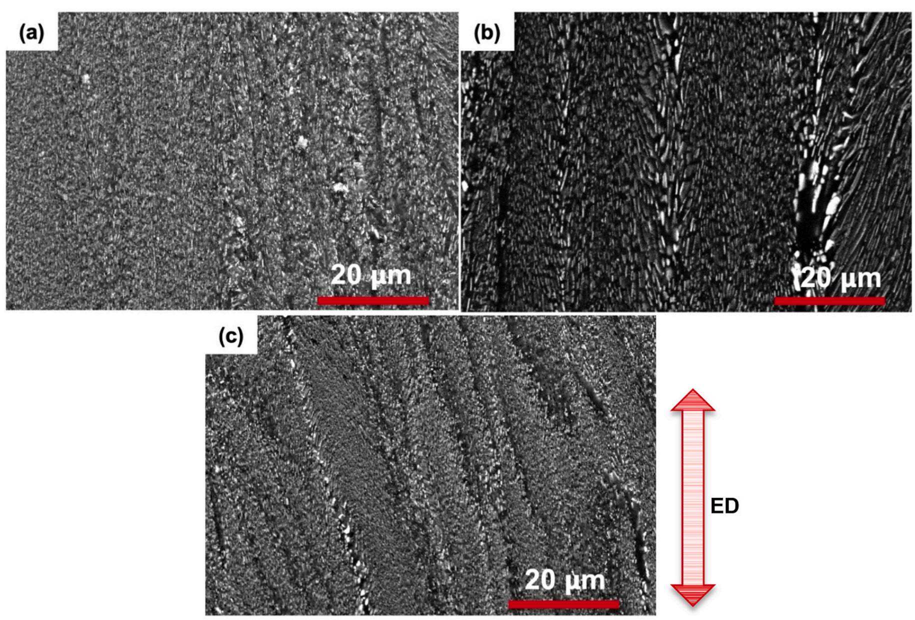

Fig. 3. Microstructure of Al-10Ce in the (a) CE, (b) CE-10, and (c) CE-100 states. The extrusion direction is shown by the red arrow and applies to all 3 panels. (For interpretation of the references to colour in this figure legend, the reader is referred to the Web version of this article.)

conditions. We observe strip-like regions oriented in the extrusion direction, with larger grains also elongated in the extrusion direction, and which are separated by finer grains. This microstructure in annealed conditions exhibits similar features, but the fine grains are distributed more uniformly throughout the microstructure. The average grain size in the extruded state is 2.06 ± 0.68 µm. The grain size distribution is shown in the Supplementary material, Fig. S1. The CE-10 and CE-100 have mean grain sizes of 2.27 ± 0.75 µm and 2.99 ± 0.72 µm, respectively, i.e annealing does not modify the grain size within the accuracy of the present measurements. The respective distributions are also shown in Fig. S1.

The average misorientation distribution is 28.93°, 26.53°, 26.40° for CE, CE-10, and CE-100, respectively. The distributions of misorientation are shown in Fig. S1 for all states. Annealing leads to a gradual shift of the misorientation distribution to lower angles. The fraction of high angle grain boundaries is 0.71, 0.65, and 0.62 for CE, CE-10, and CE-100 sample condition respectively.

The inverse pole figure, grain size distribution and the misorientation distribution of as-cast samples are shown in the Supplementary material, Fig. S2. The grain size of as cast samples is 582 ± 143.35 µm, which underlines the significant grain size reduction obtained upon extrusion. The average misorientation distribution is 11.54°, smaller than in the extruded samples.

The Grain Orientation Spread (GOS) maps for the three states are

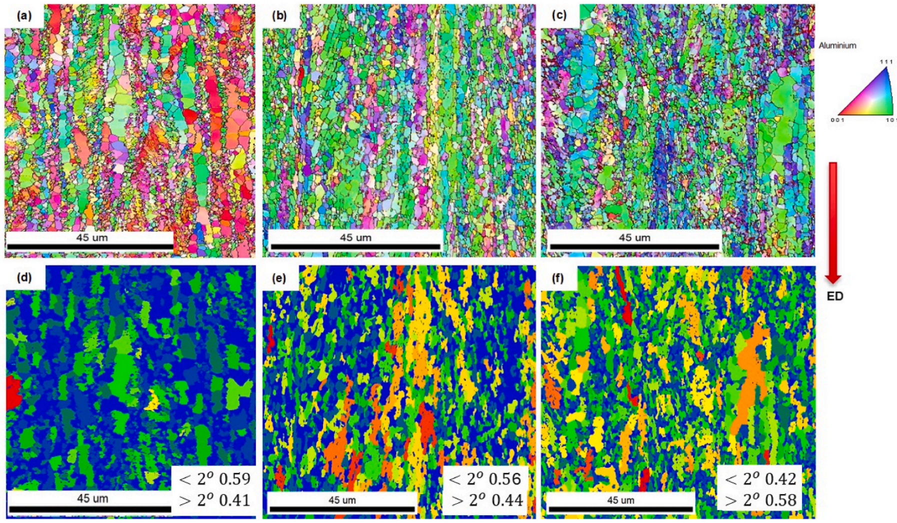

Fig. 4. IPF maps of Al-10Ce in the (a) CE, (b) CE-10, (c) CE-100 states. The GOS maps corresponding to panels (a), (b) and (c) are shown in (d), (e) and (f), respectively. Values in the legend represent grain fractions with GOS values above and below the 2° threshold.

shown in Fig. 4d–f. The fractions of grains with GOS values below and above the 2° threshold are indicated in the legend for each panel. We observe that annealing, which does not change the grain size, as discussed in the previous paragraph, leads to increasing the fraction of low angle grain boundaries.

The phase maps for the three states shown in Fig. S3. The $Al_{11}Ce_3$ phase volume fraction inferred from these images is 7 % in the extruded state and 8.2 % and 8.4 % after annealing at 300 °C for 10h and 100h, respectively. However, XRD data shown in Fig. 1 indicates no change in the height of the peaks corresponding to the intermetallic during annealing. This suggests that the non-monotonic variation obtained from EBSD (Fig. S3) is an artifact due to the limited field of view and possibly the error associated with the identification of small precipitates.

Fig. 5a–c shows the pole figure of (001), (110), and (111) projections in the CE, CE-10, and CE-100 sample conditions. The brass texture ({110}<112>)observed in the extruded sample becomes stronger after annealing for 10 h, while after annealing for 100 h the texture becomes less well defined. The maximum intensity of the pole figure is shown in Table 2. It further quantifies that the texture strengthens to some extent upon annealing for 10 h and becomes weaker after 100 h of annealing. This impacts the mechanical properties, as discussed in section 3.3. This texture evolution process entails the formation of low angle grain boundaries (evidenced by the GOS data in Fig. 4), while the total dislocation density remains largely unaffected – a conclusion emerging from the analysis presented next.

The kernel average misorientation (KAM) values of the CE, CE-10, and CE-100 are determined from the EBSD data and are used to evaluate the dislocation density. The dislocation density (geometrically necessarily dislocations), ρ_{GND}, is calculated based on the average KAM value. It is obtained using the classical strain gradient approach and is given by the following expression [28]:

$$\rho_{GND} = \frac{2\theta}{n\lambda|b_D|} \tag{1}$$

where θ is the experimentally measured KAM value, λ is the step size (1 μm), n is the number of nearest neighbors averaged in the KAM calculations (here it is 5), and b_D is the Burgers vector corresponding to the active slip system (b_D = 0.286 nm). The dislocation density values

Table 2
Grain size, maximum texture intensity, and dislocation density (obtained from XRD, ρ_{XRD} and EBSD, ρ_{GND}) for AC, CE, CE-10 and CE-100 Al-10Ce alloy.

	Grain size (μm)	Maximum Texture Intensity	Main texture component	ρ ($\times 10^{14}$ m^{-2}) XRD	ρ_{GND} ($\times 10^{14}$ m^{-2}) EBSD
AC	582	5.63	Random texture	2.92	0.10
CE	2.06	15.78	brass texture ({110}<112>)	5.56	1.16
CE-10	2.27	12.99	brass texture ({110}<112>)	2.56	0.90
CE-100	2.99	6.45	brass texture ({110}<112>)	2.94	1.40

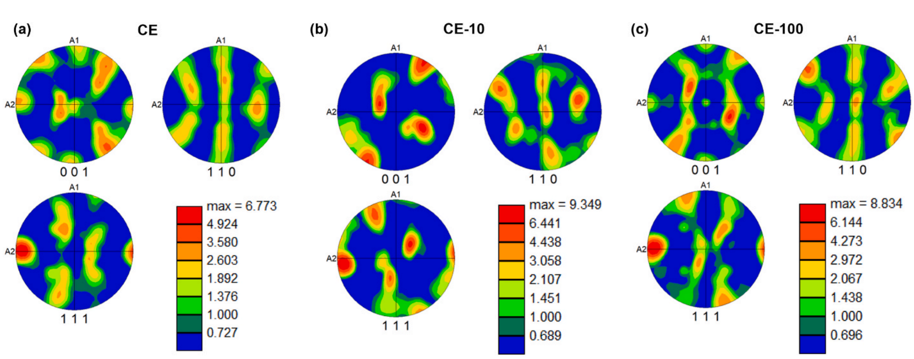

Fig. 5. Pole figure texture of (a) CE, (b) CE-10, (c) CE-100, A1 is extrusion direction and A2 is transverse direction.

obtained with Eq. (1) are shown in Table 2. The dislocation density is approximately identical in the three states of the material and takes values in the vicinity of $10^{14}\ m^{-2}$.

The XRD data is also used to calculate the dislocation density ρ using the expression [29]:

$$\rho = \frac{2\sqrt{3}\epsilon}{db_D} \tag{2}$$

where d is crystallite size, ϵ is the micro strain and $b_D = 0.286$ nm. The Williamson-Hall equation is used to determine the micro strain and crystallite size [30,31]:

$$\frac{\beta \cos\theta}{\lambda} = \frac{k}{d} + 4\epsilon \frac{\sin\theta}{\lambda} \tag{3}$$

where k is the Debye–Scherrer constant (k = 0.9), λ is the wavelength of the radiation, ($\lambda = 0.154$ nm), β is the full width at half maximum (in radian), calculated from the obtained peaks in the XRD diffractogram, Fig. 1b, and θ is the half of the Bragg angle of the respective peaks. The Williamson-Hall plot for AC and CE-100 are shown in Fig. S4. The values of ρ obtained with Eq. (2) are provided in Table 2. It is observed that $\rho > \rho_{GND}$; this can be explained by the sensitivity of each technique to the depth of probing. EBSD extracts information from 10 to 20 nm thick layer under the surface, while the thickness probed by XRD is up to several μm. However, EBSD distinguishes between geometrically necessary and stochastic dislocations, while XRD provides only an average value of the dislocation density.

We conclude from this data that extrusion produces strong microstructural refinement (both smaller grains and smaller intermetallic particle) and increased crystallographic texture. Annealing at 300 $^{\circ}C$ up to 100 h has a negligible effect on the grain and precipitate size, leaves the dislocation density unchanged, but reduces the texture. This suggests that this level of annealing should minimally impact the mechanical properties – a result discussed further in section 3.3.

3.3. Mechanical properties

In this section, we present testing results and analysis pertaining to the mechanical properties of the Al-Ce binary alloys. We consider first the effect of alloy composition and heat treatment, examining the tensile response and hardness for all three alloy compositions without any extrusion. We then focus on the eutectic alloy (Al-10Ce) and the coupled effects of extrusion and post-extrusion heat-treatment, specifically examining the AC, CE, CE-10, and CE-100 conditions. Third, we consider the elevated temperature mechanical properties, examining the response of the Al-10Ce alloy at temperatures from 150 °C to 350 °C. Finally, we examine the room temperature fracture toughness of the Al-10Ce alloy in all conditions.

3.3.1. Mechanical properties of as-cast samples

Fig. 6a shows the observed stress-strain response for 4 %, 10 % and 16%Ce in the AC, AC-10, and AC-100 conditions, without extrusion. The nominal yield stress, strength and elongation at failure are compared in Table 3. As expected, the Al-10Ce alloy exhibits the highest strength, owing to the uniform distribution of fine intermetallics of the eutectic structure. Lower strength is obtained for the hypoeutectic composition, containing a substantial fraction of primary Al (fcc), while the hypereutectic is excessively brittle due to the presence of large particles of primary $Al_{11}Ce_3$. Fig. 6a reveals that the 300 °C heat treatment has only a minor influence on tensile properties, with the highest ultimate strength observed after 100 h of exposure. The influence of microstructure indicated by the measured tensile response is further supported by the microhardness test results shown in Fig. 6b. Each value represents the average of at least 10 measurements, with the standard deviation being indicated by the error bars. For the AC condition, the average hardness was measured to be 28, 52, and 48 HV for 4, 10, and 16 wt% Ce, respectively. Similar values and variation with Ce content were observed for the AC-10 and AC-100 conditions. The excellent property retention observed in both tensile and hardness testing is consistent with the microstructure-based observations of thermal stability discussed in the preceding section.

3.3.2. Comparison of mechanical properties of as cast and extruded samples

Since the eutectic alloy Al-10Ce showed superior mechanical properties compared to the other two compositions, it was further considered for extrusion and evaluation of property retention after exposure to elevated temperatures. The room temperature engineering stress-strain curves for this alloy in the CE, CE-10, and CE-100 conditions are shown in Fig. 7a. The extruded (CE) samples showed improved mechanical properties compared to the as-cast (AC) condition. The yield stress increases three times, while the tensile strength doubles, and elongation at failure increases from 13 % to 22 %. The improvement in ductility is attributed to refinement and increased uniformity of the distribution of the $Al_{11}Ce_3$ phase caused by extrusion. We note here that the structural refinement includes both size and shape of the particles, which change from thin and interconnected lamellae to rod-like shapes of rather low aspect ratio, Fig. 3a.

Fig. 7 shows that the mechanical properties are retained after exposure to 300 °C for 10 h and 100 h, for both the ac-cast (AC) and cast/extruded (CE) alloys. Moreover, the extruded alloy experiences a modest increase in strength and ductility after 10 h of exposure, an effect not observed for the AC alloy. Considering that heat treatment does not give rise to any observable grain growth or particle coarsening, as discussed in section 3.2.2, we attribute this effect to the brass texture ({110}<112>) which develops during extrusion and after 10 h annealing (i.e. CE-10) and then becomes weaker upon long-term exposure (i.e. CE-

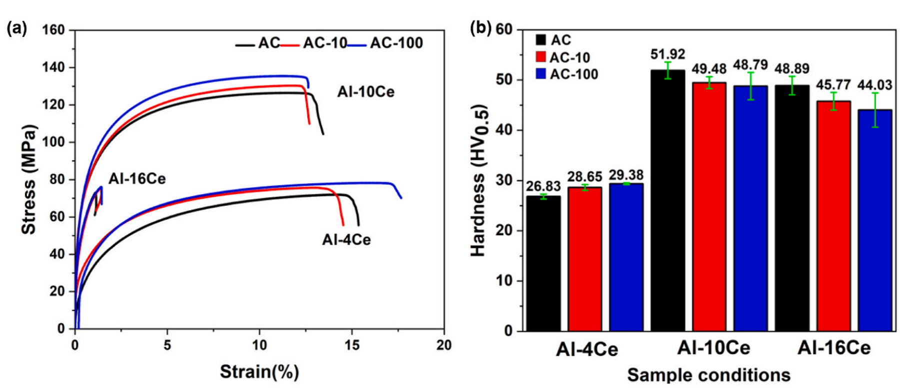

Fig. 6. (a) Nominal stress-strain curves and (b) hardness of AC, AC-10, and AC-100 specimens for Al-4Ce, Al-10Ce, and Al-16Ce.

Table 3
Tensile properties (yield stress, YS, tensile strength, UTS, and strain at failure, %El) for three alloys in AC, AC-10, and AC-100 conditions. The standard deviation is shown in brackets.

	Al-4Ce			Al-10Ce			Al-16Ce		
	AC	AC-10	AC-100	AC	AC-10	AC-100	AC	AC-10	AC-100
YS (MPa)	29.9 (0.9)	28.12 (0.8)	27.8 (0.7)	62.3 (1.5)	61.7 (1.5)	59.9 (1.8)	44.7 (2.3)	42.0 (2.5)	45.4 (2.0)
UTS (MPa)	72.1 (1.8)	75.9 (1.8)	78.3 (1.8)	126.7 (3.0)	130.6 (2.7)	135.7 (3.4)	78.9 (4.0)	79.2 (3.5)	80.2 (2.3)
%El	15.4 (0.1)	14.5 (0.2)	17.2 (0.1)	13.4 (0.1)	12.7 (0.2)	12.6 (0.8)	1.4 (0.01)	1.2 (0.01)	1.4 (0.01)

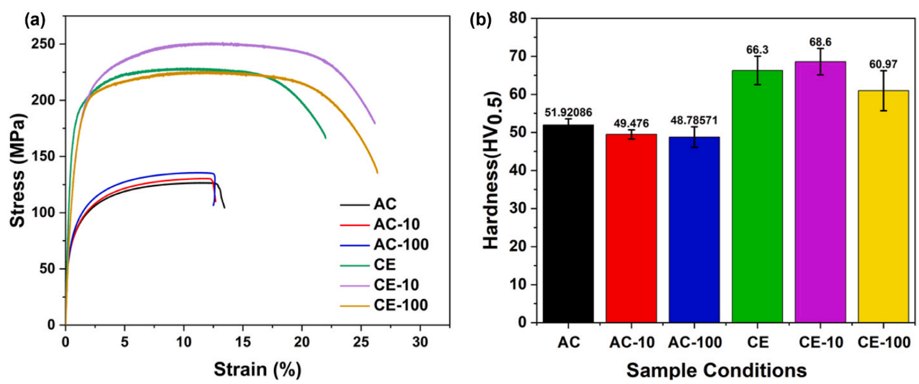

Fig. 7. (a) Engineering stress-strain curves of extruded and cast Al-10Ce samples, and (b) hardness measured at room temperature for the same set of samples. The curves in (a) are averages of 3 samples for each reported state. The hardness in (b) is computed as average of 10 measurements for each condition and the bars show the standard deviation.

100). It is prudent here to note that these assertions are based on limited initial observations and that more definitive correlation with texture evolution and the influence of extrusion deformation will require further investigation. In any event, our mechanical property measurements show that the high thermodynamic stability and resistance to coarsening of the $Al_{11}Ce_3$ precipitates provides nearly 100 % retention of the as-extruded mechanical properties during exposure to 300 °C for up to 100 h, for the Al-10Ce alloy – a finding similar to that reported for as-cast samples in section 3.3.1. Young's modulus of CE and CE-100 is ~74 GPa.

The microhardness of cast and extruded samples, before and after heat treatment, is shown in Fig. 7b. The hardness is 66.3 HV for the CE case, which is higher than the AC condition (51.92 HV) but the increase of the hardness in extruded samples compared with the cast state is smaller than the increase of the yield stress and strength, Fig. 7a. The hardness does not change upon heat treatment, within the accuracy of the present measurement. Annealing of the extruded samples at 300 °C for 100 h leads to a hardness of 60.97 HV. Longer anneals at the same temperature, of 300 h and 400 h, led to hardness values of 60.54 HV and 59 HV, respectively.

The fracture surfaces of samples subjected to tensile loading were imaged with SEM to investigate the mechanisms of failure and correlate with microstructural features. These images for Al-10Ce are shown in Fig. S5. Fracture surfaces of both cast and extruded samples contain mainly dimples. The cast samples showed some occasional shrinkage porosity. The extruded Al-10Ce alloys exhibit deeper and smaller dimples compared to as cast alloys, as shown in Figs. S5d–f. The small dimples size indicates that intense plastic deformation took place during failure. This agrees with the rather large strain at failure of 22 % of the extruded samples.

3.3.3. High temperature mechanical properties of the cast and extruded Al-10Ce alloy

The eutectic alloy (Al-10Ce) was further tested at elevated temperatures of 150 °C, 200 °C 250 °C, 300 °C and 350 °C. The stress-strain curves reported in Fig. 8a and b correspond to the AC and CE states, respectively. The yield stress and the strength are gradually decreasing with increasing temperature. We observe that the ductility does not change significantly as the temperature increases.

It is instructive to compare the temperature resistance of this alloy

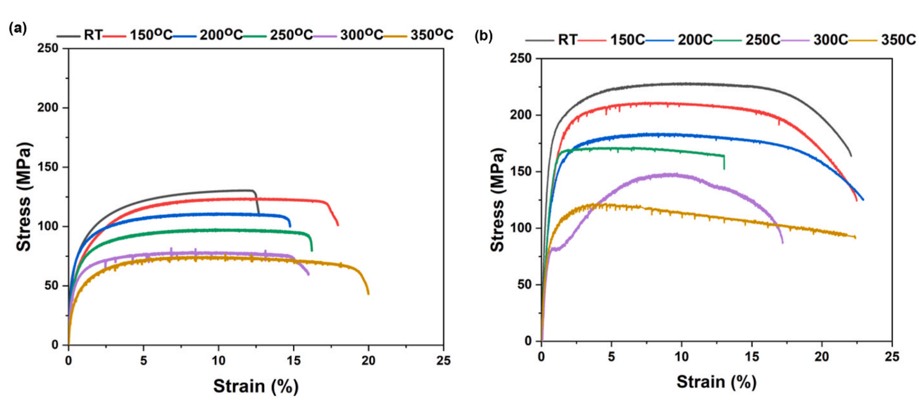

Fig. 8. Nominal stress-strain curves of Al-10Ce alloy at temperatures ranging from room temperature to 350 °C: (a) AC and (b) CE states.

with the behavior of AA2618, which is one of the commercial high temperature Al alloys. This comparison is shown in Fig. 9a, where the strength of Al-10Ce (Fig. 8) is plotted against temperature along with results from elevated temperature testing of pure Al [32,33] and AA2618 [34]. At 300 °C the tensile strength of both cast and extruded Al-10Ce is higher than the strength of AA2618. Fig. 9b shows the temperature dependence of the strength normalized by the strength at room temperature. The alloys studied in this work lose 34 % of their strength as temperature is increased to 300 °C, while AA2618 looses 90 % of its strength.

The decrease of the flow stress in Al-10Ce is due to the softening of the Al phase, while the invariance of the ductility is due to the fact that the precipitates do not evolve at these temperatures. The data in Fig. 9b supports this conjecture: consider the microstructure to be a composite of a soft phase (Al), with temperature-dependent flow stress, and a hard phase which does not flow plastically ($Al_{11}Ce_3$). In this situation, the temperature dependence of the alloy is dictated by the temperature dependence of the soft phase. The pure Al curve in Fig. 9b is parallel to the two curves corresponding to AC and CE states, which confirms the hypothesis. It is interesting to observe that, at temperatures below 150 °C, the flow stress of the alloy is temperature-independent. This is probably due to the confinement effect of the fine $Al_{11}Ce_3$ precipitates on the plastic flow of the Al matrix. At the same time, the AA2618 curve exhibits a segment parallel to the pure Al segment at temperatures below 150 °C, indicating thermal softening due to the Al "matrix," followed by an abrupt drop due to precipitate dissolution, which is followed by a third segment parallel to the pure Al curve.

The superior thermal stability of Al-10Ce compared with AA2618 can be understood based on the stability of the $Al_{11}Ce_3$ precipitates. AA2618 has alloying elements such as Cu, Si, and Mg which have relatively high solubility in Al and higher diffusion coefficients in Al than Ce at these temperatures. The solubility of Ce in Al is low, with the maximum value being less than 0.005 wt% at 642 °C. This is much lower than the solubility of Cu, Mg and Si in Al (5 wt% at 600 °C, 14.9 wt% at 451 °C and 12.5 wt% at 577 °C, respectively) [35]. The $Al_{11}Ce_3$ precipitates are thermodynamically stable up to 600 °C, while the kinetics of dissolution is also very slow due to limited Ce diffusivity [36].

3.3.4. Fracture toughness of cast and extruded Al-10Ce alloys

The fracture toughness of the eutectic cast and extruded alloy before and after annealing at 300 °C for 10 h and 100 h was measured using the single-edge bend configuration with load-line displacement measurement, in accordance with the ASTM-E1820 standard [23]. This requires evaluating the area under the force-displacement curve resulting from a 3-point bend test performed with a notched sample, up to the maximum force value, Fig. 10. The energy release rate has elastic and plastic components given by Eqs. (4) and (5) [23]:

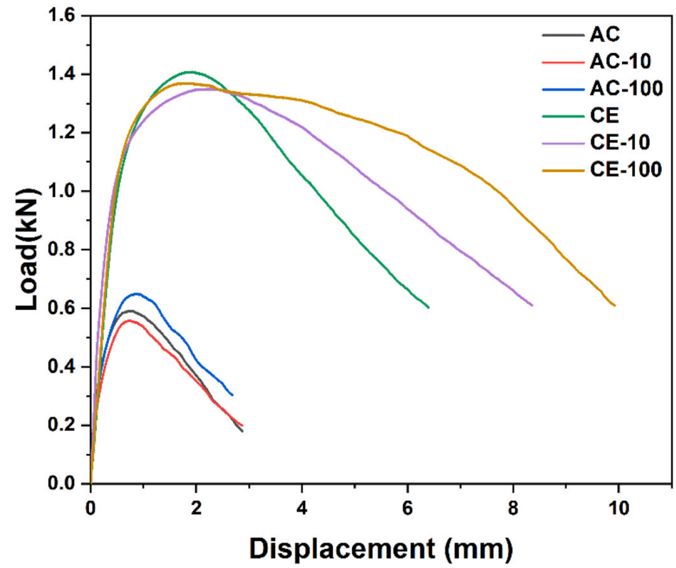

Fig. 10. Load-displacement curves of notched samples in the 3-point bend configuration of the cast and extruded Al-10Ce alloy before and after heat treatment.

$$J_{el} = \frac{K_Q^2(1-\nu^2)}{E} \tag{4}$$

$$J_{pl} = \frac{\eta_{pl}A_{pl}}{B(W-a_0)} \tag{5}$$

where K_Q is the stress intensity at fracture (i.e. maximum attained), ν and E are the Poisson's ratio and elastic modulus, respectively. Values of 0.34 and 70 GPa are used for ν and E respectively, in agreement with our test results, for the calculation of J_{el}. Further, η_{pl} is taken to be 1.9 as defined by ASTM E−1820 standard, A_{pl} is the area under the load-displacement curve up to the maximum point. S, W, B, and a_o are the span length, width, net specimen thickness, and notch length. The critical energy release rate, J_{Ic}, is evaluated as the sum of the two components of Eqs. (4) and (5) corresponding to the moment of crack growth (i.e. peak force):

$$J = J_{el} + J_{pl} \tag{6}$$

The peak load values of J_{el}, J_{pl} and J_{Ic} are shown in Table 4. The extruded samples have substantially larger toughness (55.43 J/m^2) than the as-cast samples (18.62 J/m^2). The plastic component J_{pl} is much larger than J_{el} and represents 99 % of J_{Ic}, which is expected for a ductile

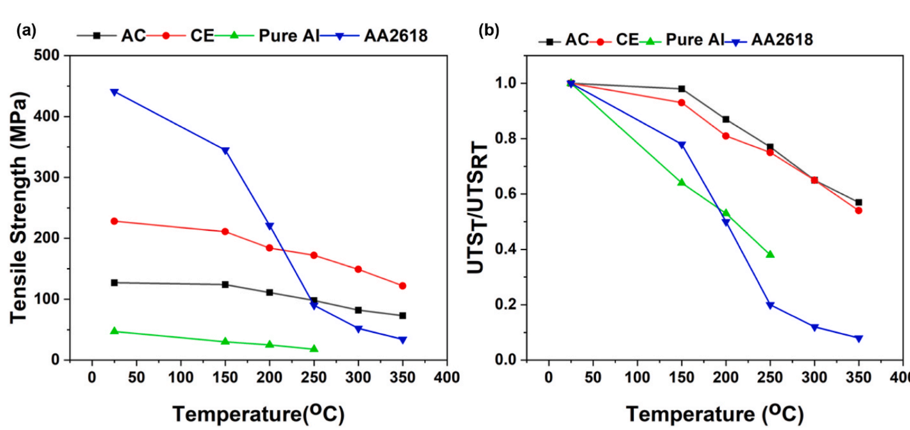

Fig. 9. (a) Temperature dependence of the strength, UTS, and (b) ratio of UTS normalized by UTS at room temperature for Al-10Ce in AC, CE, pure Al and AA2618.

Table 4
Values of J_{el}, J_{pl} and J_{Ic} for cast and extruded samples, before and after annealing.

	Load (N)	J_{el} (kJ/m^2)	J_{pl} (kJ/m^2)	$J = J_{el} + J_{pl}$ (kJ/m^2)
AC	591	0.57	18.05	18.62
AC-10	558	0.51	14.72	15.23
AC-100	650	0.68	19.22	19.90
CE	1408	0.058	55.36	55.42
CE-10	1349	0.045	43.28	43.33
CE-100	1369	0.10	54.02	54.12

metallic alloy. The annealed samples show similar fracture toughness values as compared to their non-heat treated counterparts in both cast and extruded conditions which, again, underscores the microstructural stability of this alloy. The highest fracture toughness (J_{Ic}) values are reported in Al alloys for the wire-arc DED-processed Al-Si, which is 36.8 kJ/m^2 [37]; Al-Li alloys have J_{Ic} value of ~26 kJ/m^2 [38].

The important observation beyond the insensitivity to annealing supported by the other data reported here and, in the literature, is the drastic simultaneous increase of the toughness, strength and ductility of the alloy upon extrusion.

3.4. Strengthening mechanisms and ductility of extruded samples

The strengthening mechanisms operating in these alloys include grain size strengthening, strain hardening and strengthening due to the presence of the fine $Al_{11}Ce_3$ dispersion. Solid solution strengthening is precluded by the low solubility of Ce in Al. The contribution of the strengthening mechanisms is considered the be additive, which implies the assumption of them acting independently [27,39]:

$$\sigma_y = \sigma_{dis} + \sigma_d + \sigma_{gs}, \tag{7}$$

where, σ_y is the yield stress, σ_{dis} is the contribution of dispersion strengthening, σ_d corresponds to strain hardening, and σ_{gs} accounts for the effect of grain boundaries (Hall-Petch effect). Grain size strengthening is expressed by the Hall-Petch relation [40]:

$$\sigma_{gs} = \sigma_o + kd^{-0.5}, \tag{8}$$

Where σ_o is the lattice friction (Peierls stress), the grain size d is evaluated based on the EBSD results, Table 2, and k is the Hall-Petch coefficient with a value of 0.07 MPa m$^{0.5}$ [41]. σ_o is considered equal to 20 MPa, which is the yield stress of pure Al.

Strain hardening results from interaction and multiplication of dislocations during plastic deformation. The contribution of dislocation strengthening (i.e. strain hardening) can be calculated using the Taylor equation [42]:

$$\sigma_d = M\alpha b_D G\rho^{0.5}, \tag{9}$$

where M is the Taylor factor, with a value of 2.94 for Al [43], α is the strength coefficient with a value of 0.24 [44], b_D is the Burgers vector (b_D = 0.286 nm), G is the shear modulus (G = 26 GPa) for pure Al, and ρ is the dislocation density evaluated based on EBSD and reported in Table 2.

The dispersoid number density and, to a smaller extent, their shape and distribution, define the contribution of σ_{dis} to the total flow stress [27,45]. In this study, we use Eq. (7) along with Eqs. (8) and (9) to infer the contribution of σ_{dis} to the measured yield stress. Therefore, σ_{dis} is calculated as:

$$\sigma_{dis} = \sigma_y - \sigma_{gs} - \sigma_d. \tag{10}$$

The contributions of the various strengthening mechanisms are listed in Table 5 for cast and extruded Al-10Ce before and after annealing. The percentage contribution to the total yield stress of each mechanism is indicated in parentheses.

Table 5
Contribution of grain size strengthening, σ_{gs}, strain hardening, σ_d, and dispersoid strengthening, σ_{dis}, to the yield stress of Al-10Ce cast and extruded samples before and after annealing. The fraction of the respective contribution to the total yield stress is reported in parentheses for each case and mechanism.

	σ_{gs} (MPa)	σ_d (MPa)	σ_{dis} (MPa)
AC	22.9 (36.8 %)	16.6 (26.6 %)	22.8 (36.6 %)
CE	68.8 (39.1 %)	56.5 (32.1 %)	50.7 (28.8 %)
CE-10	66.5 (34.1 %)	49.8 (25.5 %)	78.7 (40.4 %)
CE-100	60.5 (34 %)	62.1 (34.9 %)	55.4 (31.1 %)

The as-cast alloy has large grains and relatively low dislocation density, which implies a low yield stress. The contribution of σ_{dis} to the yield stress results comparable with that of the grain size strengthening mechanism. The as extruded (CE) and annealed alloys (CE-10, CE-100) have larger yield stress and larger σ_{gs}, σ_d and σ_{dis} compared with AC. The grain size mechanism, σ_{gs}, makes the largest contribution to the yield stress. Since the grain size and dislocation densities in these alloys are not very sensitive to annealing, the contributions of these mechanisms to the yield stress are largely independent of the annealing state. An exception is observed in the case of CE-10 where σ_d is smaller due to the lower dislocation density (ρ_{GND} in Table 2 was used for this evaluation). This is compensated by σ_{dis}, which is larger than the values reported for CE and CE-100. However, in broad terms, the contribution to the yield stress of the three strengthening mechanisms is somewhat similar (each contributes approximately 1/3 of the yield stress), which is surprising given their very different microstructures.

4. Conclusion

This study focuses on the effect of extrusion on the structure, mechanical properties and thermal stability of Al-Ce binary alloys. The as cast alloys have large grain size, relatively low yield stress and strength, but strong thermal stability arising from the low solubility and diffusivity of Ce in Al (fcc). Extrusion leads to substantial refinement of the microstructure, involving both the Al (fcc) grain size and the $Al_{11}Ce_3$ intermetallic particle size. Relative to the as-cast state, extrusion results in larger yield strength, ultimate tensile strength, and elongation by factors of 3, 2, and 2, respectively. Moreover, because these gains are largely attributed to the $Al_{11}Ce_3$ structure, these properties are preserved upon annealing at 300^{o}C for up to 100 h. The toughness also more than doubles in the extruded states relative to the as cast state, irrespective of the annealing applied. Testing at elevated temperatures indicates that the strength decreases as the test temperature increases, but this decrease is much less pronounced than in existing commercial Al alloys considered to be temperature-resistant. This indicates that adequate processing leading to microstructural refinement may render this class of alloys useful in applications in which high temperature resistance is required.

The data resulting from this investigation is included in the article.

CRediT authorship contribution statement

Gaurav Singh: Writing – original draft, Methodology, Investigation, Formal analysis, Data curation. **Humphrey Wara Odhiambo:** Methodology, Investigation, Formal analysis, Data curation. **Mohamad Hasan Bin Tasneem:** Investigation, Formal analysis, Data curation. **Gaoyuan Ouyang:** Writing – review & editing, Supervision, Project administration, Methodology, Funding acquisition, Formal analysis, Conceptualization. **Monica A. Soare:** Writing – review & editing, Funding acquisition, Formal analysis, Conceptualization. **Jun Cui:** Supervision, Project administration, Funding acquisition, Formal analysis, Conceptualization. **Ralph E. Napolitano:** Writing – review & editing, Supervision, Project administration, Funding acquisition, Formal analysis, Conceptualization. **Catalin R. Picu:** Writing – review & editing, Supervision, Project administration, Investigation, Funding acquisition, Formal analysis, Conceptualization.

Declaration of competing interest

The authors have no conflict of interest or competing interests to declare.

Acknowledgement

This work was supported by the US Department of Energy (DOE) through Grant No. DE-EE0010219.

Appendix A. Supplementary data

Supplementary data to this article can be found online at https://doi.org/10.1016/j.msea.2024.147395.

Data availability

The data produced by this research is embedded in the article.

References

[1] Y.H. Gao, C. Yang, J.Y. Zhang, L.F. Cao, G. Liu, J. Sun, E. Ma, Stabilizing nanoprecipitates in Al-Cu alloys for creep resistance at 300°C, Mater Res Lett 7 (2019) 18–25, https://doi.org/10.1080/21663831.2018.1546773.

[2] S. Mondol, T. Alam, R. Banerjee, S. Kumar, K. Chattopadhyay, Development of a high temperature high strength Al alloy by addition of small amounts of Sc and Mg to 2219 alloy, Mater. Sci. Eng., A 687 (2017) 221–231, https://doi.org/10.1016/J.MSEA.2017.01.037.

[3] Z. Huda, P. Edi, Materials selection in design of structures and engines of supersonic aircrafts: a review, Mater. Des. 46 (2013) 552–560, https://doi.org/10.1016/J.MATDES.2012.10.001.

[4] S.O. Rogachev, E.A. Naumova, Thermal stability of Al-Ca and Al-Ce alloys obtained by high-pressure torsion, J. Mater. Eng. Perform. 30 (2021) 9192–9199, https://doi.org/10.1007/s11665-021-06105-4.

[5] S. Shen, C. Wu, Y. Li, Y. Huang, W. Huang, P. Zhang, S. Zhong, Y. Lu, G. Luo, Z. Gan, J. Liu, Refining mechanism and elevated-temperature mechanical properties of Al-Ce alloys solidified under super gravity field, Mater. Sci. Eng., A 879 (2023), https://doi.org/10.1016/j.msea.2023.145191.

[6] Y. Guo, J. Hu, Q. Han, B. Sun, J. Wang, C. Liu, Microstructure diversity dominated by the interplay between primary intermetallics and eutectics for Al-Ce heat-resistant alloys, J. Alloys Compd. 899 (2022), https://doi.org/10.1016/j.jallcom.2021.162914.

[7] E.T. Stromme, H.B. Henderson, Z.C. Sims, M.S. Kesler, D. Weiss, R.T. Ott, F. Meng, S. Kassoumeh, J. Evangelista, G. Begley, O. Rios, Ageless aluminum-cerium-based alloys in high-volume die casting for improved energy efficiency, JOM 70 (2018) 866–871, https://doi.org/10.1007/s11837-018-2861-9.

[8] G.S. Cole, A.M. Sherman, Light weight materials for automotive applications, Mater. Char. 35 (1995) 3–9, https://doi.org/10.1016/1044-5803(95)00063-1.

[9] B. Stojanovic, M. Bukvic, I. Epler, Application of aluminum and aluminum alloys in engineering, Applied Engineering Letters 3 (2018) 2466–4847, https://doi.org/10.18485/aeletters.2018.3.2.2.

[10] F. Czerwinski, Cerium in aluminum alloys, J. Mater. Sci. 55 (1 55) (2019) 24–72, https://doi.org/10.1007/S10853-019-03892-Z, 2019.

[11] D. Weiss, Improved high-temperature aluminum alloys containing cerium, J. Mater. Eng. Perform. 28 (2019) 1903–1908, https://doi.org/10.1007/s11665-019-3884-2.

[12] Z.C. Sims, O.R. Rios, D. Weiss, P.E.A. Turchi, A. Perron, J.R.I. Lee, T.T. Li, J. A. Hammons, M. Bagge-Hansen, T.M. Willey, K. An, Y. Chen, A.H. King, S. K. McCall, High performance aluminum-cerium alloys for high-temperature applications, Mater. Horiz. 4 (2017) 1070–1078, https://doi.org/10.1039/c7mh00391a.

[13] F. Czerwinski, The growth of quaternary divorced eutectic in Al–Ce–Si–Mg alloys, Metall Mater Trans A Phys Metall Mater Sci 54 (2023) 391–398, https://doi.org/10.1007/s11661-022-06911-y.

[14] F. Czerwinski, B.S. Amirkhiz, On the Al-Al11Ce3 eutectic transformation in aluminum-cerium binary alloys, Materials 13 (2020) 1–27, https://doi.org/10.3390/ma13204549.

[15] J. Ye, K. Dai, M. Gao, J. Chen, R. Guan, Primary phase transformation mechanism in a hypereutectic Al-Ce alloy during rapid solidification, Mater. Lett. 340 (2023), https://doi.org/10.1016/j.matlet.2023.134172.

[16] W. Wang, Q. Pan, G. Lin, X. Wang, Y. Sun, X. Wang, J. Ye, Y. Sun, Y. Yu, F. Jiang, J. Li, Y. Liu, Microstructure and properties of novel Al-Ce-Sc, Al-Ce-Y, Al-Ce-Zr and Al-Ce-Sc-Y alloy conductors processed by die casting, hot extrusion and cold drawing, J. Mater. Sci. Technol. 58 (2020) 155–170, https://doi.org/10.1016/j.jmst.2020.03.073.

[17] S.O. Rogachev, E.A. Naumova, E.A. Lukina, A.V. Zavodov, V.M. Khatkevich, High strength al–la, al–ce, and al–ni eutectic aluminum alloys obtained by high-pressure torsion, Materials 14 (2021), https://doi.org/10.3390/ma14216404.

[18] Z.C. Sims, O.R. Rios, D. Weiss, P.E.A. Turchi, A. Perron, J.R.I. Lee, T.T. Li, J. A. Hammons, M. Bagge-Hansen, T.M. Willey, K. An, Y. Chen, A.H. King, S. K. McCall, High performance aluminum-cerium alloys for high-temperature applications, Mater. Horiz. 4 (2017) 1070–1078, https://doi.org/10.1039/c7mh00391a.

[19] W. Wang, Q. Pan, G. Lin, X. Wang, Y. Sun, X. Wang, J. Ye, Y. Sun, Y. Yu, F. Jiang, J. Li, Y. Liu, Microstructure and properties of novel Al-Ce-Sc, Al-Ce-Y, Al-Ce-Zr and Al-Ce-Sc-Y alloy conductors processed by die casting, hot extrusion and cold drawing, J. Mater. Sci. Technol. 58 (2020) 155–170, https://doi.org/10.1016/j.jmst.2020.03.073.

[20] D.S. Voroshilov, S.B. Sidelnikov, V.M. Bespalov, R.E. Sokolov, T.V. Bermeshev, V. A. Berngardt, S.N. Lezhnev, A.V. Durnopyanov, A.A. Kovaleva, I.L. Konstantinov, O.S. Novikova, M.M. Motkov, Combined rolling-extrusion of various billets from the Al–Ce–La alloy for electrical wire production, Int. J. Adv. Des. Manuf. Technol. 131 (2024) 4699–4725, https://doi.org/10.1007/s00170-024-13339-8.

[21] A. E8/E8M, Standard Test Methods for Tension Testing of Metallic Materials, ASTM International, 2013.

[22] A. E384-17, Standard test method for microindentation hardness of materials. https://doi.org/10.1520/E0384-17, 2016.

[23] F.M. Testing. ASTM Standard E1820-11. Standard Test Method for Measurement of Fracture Toughness, 2009. https://www.astm.org/e1820-11.html.

[24] S. El-Hadad, M.E. Moussa, M. Shoeib, Influence of Al11Ce3 size and distribution on the electrochemical properties of sonoprocessed Al-10 wt.% Ce alloy, Int. J. Metalcast. 17 (2023) 1606–1614, https://doi.org/10.1007/s40962-022-00870-1.

[25] Y. Sun, C. Hung, R.J. Hebert, C. Fennessy, S. Tulyani, M. Aindow, Eutectic microstructures in dilute Al-Ce and Al-Co alloys, Mater. Char. 154 (2019) 269–276, https://doi.org/10.1016/j.matchar.2019.06.010.

[26] Y. Wang, X. Liang, L. Zeng, H. Wu, H. Li, The microstructure evolution of Al-5Ce alloy prepared by strain-induced melt activation during semi-solid isothermal treatment process, Mater. Lett. 326 (2022), https://doi.org/10.1016/j.matlet.2022.132948.

[27] C. Zhang, Y. Wang, H. Lv, H. Gao, J. Wang, B. Sun, Enhanced load transfer and ductility in Al–9Ce alloy through heterogeneous lamellar microstructure design by cold rolling and annealing, Mater. Sci. Eng., A 821 (2021), https://doi.org/10.1016/j.msea.2021.141591.

[28] I. Basu, V. Ocelík, J.T.M. De Hosson, BCC-FCC interfacial effects on plasticity and strengthening mechanisms in high entropy alloys, Acta Mater. 157 (2018) 83–95, https://doi.org/10.1016/J.ACTAMAT.2018.07.031.

[29] G.K. Williamson, R.E. Smallman III, Dislocation densities in some annealed and cold-worked metals from measurements on the X-ray debye-scherrer spectrum, Phil. Mag. 1 (1956) 34–46, https://doi.org/10.1080/14786435608238074.

[30] Z. Zribi, H.H. Ktari, F. Herbst, V. Optasanu, N. Njah, EBSD, XRD and SRS characterization of a casting Al-7wt%Si alloy processed by equal channel angular extrusion: dislocation density evaluation, Mater. Char. 153 (2019) 190–198, https://doi.org/10.1016/j.matchar.2019.04.044.

[31] S.C. Wang, Z. Zhu, M.J. Starink, Estimation of dislocation densities in cold rolled Al-Mg-Cu-Mn alloys by combination of yield strength data, EBSD and strength models, J. Microsc. 217 (2005) 174–178, https://doi.org/10.1111/j.1365-2818.2005.01449.x.

[32] J.G. Kaufman, Properties of pure aluminum, aluminum science and technology, 31–43, https://doi.org/10.31399/ASM.HB.V02A.A0006505, 2018.

[33] A.H. Committee, Properties and selection: nonferrous alloys and special-purpose materials, properties and selection: nonferrous alloys and special-purpose materials. https://doi.org/10.31399/ASM.HB.V02.9781627081627, 1990.

[34] 2618 and 2618A, Al-Cu-Mg-Ni alloys for high-temperature service, properties and selection of aluminum alloys, 328–329, https://doi.org/10.31399/ASM.HB.V02B.A0006616, 2019.

[35] C. Weiping, Diffusion of cerium in the aluminium lattice, J. Mater. Sci. Lett. 16 (1997) 1824–1826, https://doi.org/10.1023/A:1018572803223/METRICS.

[36] H. Okamoto, Al-Ce (Aluminum-Cerium), J. Phase Equilibria Diffus. 32 (2011) 392–393, https://doi.org/10.1007/S11669-011-9914-X/TABLES/1.

[37] M.J. Paul, T. Klein, C. Simson, J. Niedermayer, J.J. Kruzic, B. Gludovatz, Strength and fracture resistance of in-situ alloyed compositionally-graded Al-Si processed by dual-wire arc directed energy deposition, Addit. Manuf. 60 (2022) 103291, https://doi.org/10.1016/j.addma.2022.103291.

[38] S.P. Lynch, R.J.H. Wanhill, R.T. Byrnes, G.H. Bray, Fracture toughness and fracture modes of aerospace aluminum–lithium alloys, in: Aluminum-Lithium Alloys, Elsevier, 2014, pp. 415–455, https://doi.org/10.1016/B978-0-12-401698-9.00013-6.

[39] R. Gope, S. Mondol, S. Ganguly, A. Mandal, Microstructure and mechanical properties of suction-cast aluminium–cerium alloys, Mater. Sci. Technol. 39 (2023) 2824–2841, https://doi.org/10.1080/02670836.2023.2228056.

[40] S. Bolognesi, D. Tong, The deformation and ageing of mild steel: III discussion of results, Proc. Phys. Soc. B 64 (1951) 747, https://doi.org/10.1088/0370-1301/64/9/303.

[41] Z.N. Farhat, Y. Ding, D.O. Northwood, A.T. Alpas, Effect of grain size on friction and wear of nanocrystalline aluminum, Mater. Sci. Eng., A 206 (1996) 302–313, https://doi.org/10.1016/0921-5093(95)10016-4.

[42] N. Hansen, X. Huang, Microstructure and flow stress of polycrystals and single crystals, Acta Mater. 46 (1998) 1827–1836, https://doi.org/10.1016/S1359-6454(97)00365-0.

[43] H. Mecking, U.F. Kocks, C. Hartig, Taylor factors in materials with many deformation modes, Scripta Mater. 35 (1996) 465–471, https://doi.org/10.1016/1359-6462(96)00137-6.
[44] M.E. Kassner, Taylor hardening in five-power-law creep of metals and Class M alloys, (n.d.). https://doi.org/10.1016/j.actamat.2003.08.019.
[45] N.Q. Vo, D.C. Dunand, D.N. Seidman, Improving aging and creep resistance in a dilute Al-Sc alloy by microalloying with Si, Zr and Er. https://doi.org/10.1016/j.actamat.2013.10.008, 2013.